Astron. Astrophys. 320, 378–394 (1997)

ASTRONOMY AND ASTROPHYSICS

ROSAT observations of the galactic wind in M 82

D.K. Strickland, T.J. Ponman, and I.R. Stevens

School of Physics and Space Research, The University of Birmingham, Edgbaston, Birmingham, B15 2TT, UK

Received 5 March 1996 / Accepted 22 July 1996

Abstract. We present *ROSAT* PSPC and HRI observations of the galactic wind from the starburst galaxy M 82. X-ray emission from the wind is detected to a distance of ~ 6 kpc from the plane of the galaxy. Making use of the PSPC's mixture of good spatial and spectral characteristics, we separate point source and diffuse emission, and investigate the spectral variation of the diffuse emission through the wind. The intrinsic X-ray luminosity of the wind in the 0.1-2.4 keV band is found to be approximately 1.9×10^{40} erg s^{-1} outside the immediate vicinity of the nucleus. The temperature of the diffuse emission is found to decrease weakly from ~ 0.6 keV to ~ 0.4 keV along the minor axis, whilst the inferred gas density drops as $z^{-0.5}$ and $z^{-0.8}$ along the northern and southern minor axes respectively. We compare these results with those expected from two simple models for the emission: Chevalier & Clegg's adiabatically expanding free wind and emission from shocked clouds in a wind, and find that the emission cannot come from a free wind, but that shock heated clouds could be the source of the emission.

Key words: galaxies: individual: M 82 – galaxies: starburst – galaxies: ISM-galaxies: halos – X-rays: galaxies

1. Introduction

Only within the last two decades has it been realised that the interplay between vigorous star formation and the state of the interstellar medium (ISM) can have profound implications for the evolution of galaxies and their environments (see for example Norman & Ikeuchi 1989). Starbursts, and in particular the galactic mass outflows or winds driven by thermalised stellar winds from massive stars and supernovae, have implications for systems of all sizes. Galactic winds may be responsible for the destruction of dwarf galaxies (Dekel & Silk 1986; Heckman et al. 1995), enrichment of the ICM and IGM in clusters and groups and removal of gas from merger remnants.

Heckman et al. (1993) provide a comprehensive review of the observational data and theory of galactic winds. Briefly, thermalised kinetic energy from stellar winds and supernovae from massive stars in the starburst creates a hot ($\sim 10^8$ K) bubble in the ISM. This expands, sweeping up ambient material into a dense shell. Eventually the bubble breaks out of the disk of the galaxy along the minor axis. The hot wind then escapes freely at several thousand kilometers per second. The dense shell fragments due to Rayleigh-Taylor instabilities, and is carried along by the wind at velocities of order hundreds of kilometers per second. This or ambient clouds overrun by the wind is the source of optical emission line filaments, and possibly the soft X-ray emission.

The archetypal starburst M 82 presents possibly the best test case, given its proximity (3.63 Mpc, Freedman et al. 1994) and the wealth of observational data available. Its high infrared luminosity ($L_{IR} = 4 \times 10^{10}\, L_\odot$, Rieke et al. 1993), disturbed morphology, population of supernova remnants (Muxlow et al. 1994) and luminous young super star clusters (O'Connell et al. 1995) are all signatures of a strong burst of star formation. The starburst was probably caused by a close interaction with M 82's nearby (projected distance ~ 40 kpc) neighbour M81 about 2×10^8 yr ago (Cottrell 1977), and a tidal bridge of HI connects the two galaxies (Yun et al. 1993).

A set of emission line filaments along M 82's minor axis show velocities consistent with gas motions along the surface of a cone at $v = 600$ km s^{-1} (Axon & Taylor 1978): cooler material swept out of the galaxy by the much hotter wind. The Hα emission defines an outflow that has a radius ~ 440 pc at a distance of $z \sim 180$ pc above the galactic plane (Götz et al. 1990), and is approximately cylindrical for $z < 350$ pc. At larger z the blowout flares out to a cone with an opening angle $\theta \approx 30°$ (see Fig. 5 in McKeith et al. 1995). Within 1 kpc of the nucleus the inferred electron density in the filaments decreases with increasing z. McKeith et al. (1995) claim this is consistent with a $\rho \propto z^{-2}$ model, as would be expected if the Hα filaments were in pressure equilibrium with freely expanding wind such as that proposed by Chevalier & Clegg (1985). A similar density decrease was also inferred by McCarthy et al. (1987).

Additional evidence for a galactic wind is the synchrotron emitting radio halo, extended preferentially along the minor axis (Seaquist & Odegard 1991), due to relativistic electrons from supernovae swept out from the starburst region by the wind. This has a maximum extent comparable to the X-ray emission (this paper). A steepening of the spectral index interpreted as aris-

Send offprint requests to: D.K. Strickland

ing from energy loss by Inverse Compton (IC) scattering of the electrons off IR photons, allows an estimate of the speed with which the electrons are being convected outwards, assuming re-acceleration in shocks to be negligible. Seaquist and Odegard (1991) claim a conservative estimate of the wind velocity, allowing for the uncertainties, lies in the range 1000-3000 $\mathrm{km\,s^{-1}}$, similar to that predicted from theory (Chevalier & Clegg 1985; Heckman et al. 1993).

Schaaf et al.'s (1989) suggestion that X-rays produced by this IC scattering could be the source of the observed X-ray emission is argued against by Seaquist et al. (1991) who predict $L_{\rm IC} = 10^{38}\,\mathrm{erg\,s^{-1}}$, in contrast with the value we derive below of $2 \times 10^{40}\,\mathrm{erg\,s^{-1}}$ in the *ROSAT* band.

X-ray observations should provide a direct method of testing the galactic wind paradigm, given that thermalised stellar wind and supernovae ejecta is expected to have a temperature of $\sim 10^8$ K. Previous X-ray observations of M 82 have suffered from poor sensitivity, poor spectral resolution and to a lesser extent poor spatial resolution. Watson et al. (1984) detected several very luminous ($\sim 10^{39}\,\mathrm{erg\,s^{-1}}$) sources along with diffuse emission using the *Einstein* HRI. The diffuse emission was seen to extend out to $\sim 3'$ (~ 3 kpc) to the south-east and $\sim 2'$ to the north-west. Spectral fits using the *Einstein* IPC and MPC were inconclusive in that they were unable to distinguish between a power law or a thermal origin for the emission. Given that they were unable to separate the point sources and the diffuse emission, this is not surprising.

A reanalysis of the *Einstein* data by Fabbiano (1988) did attempt to separate the different components. The MPC (without any imaging capability) fitted temperature of $6.8^{+5.7}_{-2.3}$ keV would be dominated by the nuclear source and hence is not an estimate of the wind temperature. The IPC gives $T \sim 1.2$ keV for the emission within $3'$ of the nucleus, compared to ~ 2.7 keV for the emission between 200-300″. The radial surface brightness in the IPC falls off approximately as r^{-3}, consistent with the expectation for a free wind.

Schaaf et al. (1989) use an *EXOSAT* observation together with the *Einstein* data. The *EXOSAT* spectrum is consistent with either a power law or a Raymond & Smith plasma with temperature 9^{+9}_{-4} keV, again without any separation of point source and diffuse components.

Although the extent of the emission seen within the *EXOSAT* and *Einstein* observations compares well with the higher sensitivity observation of *ROSAT* (Fig. 1), Tsuru et al. (1990) from observations with Ginga, claim evidence for a very extended, 100 kpc halo. Two north-south scans of a 5° region centred on M 82 show excess flux to the north of M 82, but not to the south. A spectral fit to this emission is essentially unconstrained, with a temperature in the range 1-11 keV. Tsuru et al. argue that a single point source could not produce the observed feature, as the position of the extra source is inconsistent between the two scans. They concede this could be due to two or more point sources, but estimate the chance of finding two sources of suitable flux in such a small region as 4 square degrees is $< 5\%$. The dynamical age of such a halo is $\sim 10^8$ yr, hence this might be the remains of a wind from a starburst $\sim 10^8$ yr ago.

The *ROSAT* HRI observations of M 82 (Bregman et al. 1995) show three sources within the nuclear region of M 82, although two of them have very low S/N values above the strong and spatially varying wind emission. A very bright source present in the *Einstein* data appears to have faded away completely (Collura et al. 1994), although the main nuclear source is at a position consistent with the *Einstein* observation.

Bregman et al. (1995)analyse the diffuse emission without the benefit of any spectral information. They conclude that the extended emission along the minor axis is consistent with an outflow of gas with opening angle that decreases with increasing radius within $1.7'$ of the nucleus and at constant opening angle at larger radii. They model the emission successfully by adiabatically expanding gas of constant mass flux, and predict a decrease in temperature of the gas with increasing radius.

We report below, an analysis of the *ROSAT* PSPC and HRI observations of this X-ray emission. The PSPC's mixture of good spatial and spectral capabilities compared to any other X-ray instrument, allow the best determination yet of the properties of this emission. In particular, we can separate point source and diffuse emission, and investigate the variation of spectral properties as a function of distance from the nucleus. For the first time, we show that the diffuse emission is thermal in origin, and obtain temperatures, emission measures, metallicities, and, for an assumed geometry, electron densities, gas masses and total energies. We compare our results with Chevalier & Clegg's (1985) analytical model of a galactic wind, and a simple model in which the emission comes from shock heated clouds rather than the wind itself. Our results allow us to reject the possibility that the X-ray emission comes from the wind itself, and show that it could be consistent with emission from shock heated clouds.

2. Data reduction

M 82 was observed three times early in the *ROSAT* mission (Trümper 1984) by both the PSPC and the HRI (Table 1). Only the PSPC and the longer of the two HRI observations are used in the present analysis. The use of the HRI's good spatial resolution ($\sim 5''$ FWHM) to complement the spectral information available at moderate resolution ($27''$ at 1 keV) from the PSPC, is advantageous, especially with regard to clarifying source confusion. The data sets were obtained from the Leicester Data Archive (LEDAS) and were analysed using the Starlink *ASTERIX* X-ray analysis system.

2.1. Background subtraction of PSPC data

The data were cleaned of periods of high background (both particle and Solar) and poor pointing stability, leaving 21194 seconds of good data. A spectral image (or *data cube*) was formed over a $0.3° \times 0.3°$ region centred on the 2.2μm nucleus, with a pixel size of $5''$ and 22 energy bins between channel numbers 11 and 230 (corresponding to roughly 0.11-2.3 keV). A model of the background was constructed using data from an annulus $r = 0.15° - 0.25°$, centred on M 82, with contaminating

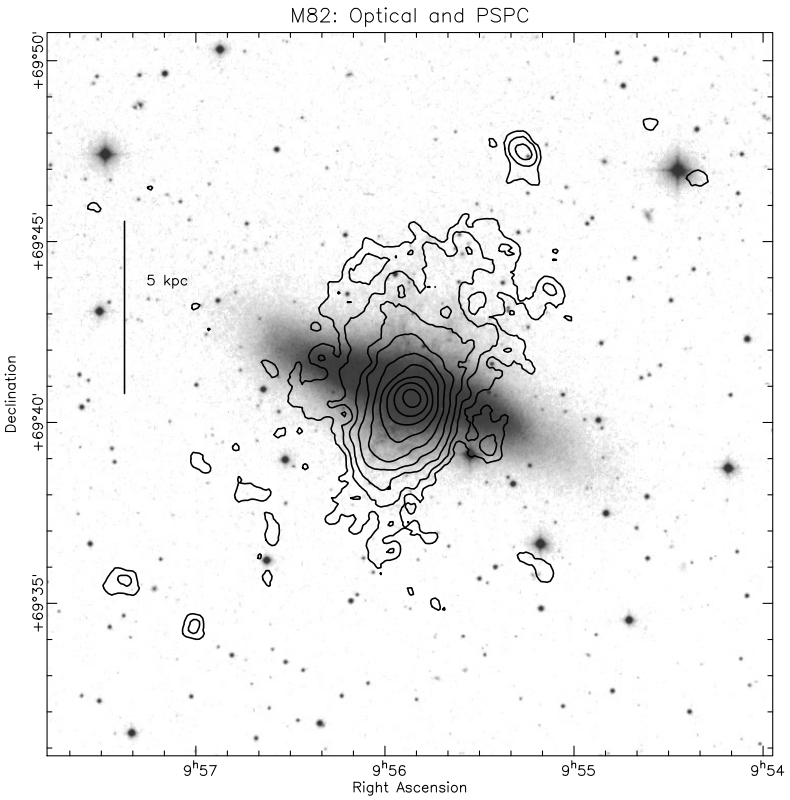

Fig. 1. Contours of X-ray emission (0.1–2.4 keV) from the PSPC overlaid on a digitised sky-survey optical image of M 82. The X-ray emission has been lightly smoothed with a Gaussian of standard deviation $\sigma = 10''$ to suppress noise. The contour levels increase in factors of two from 2.88×10^{-3} cts s^{-1} arcmin^{-2} ($\sim 3\sigma$ above the background).

Table 1. ROSAT observations of M 82. Although the first HRI observation rh600021 was ostensibly taken within a couple of days of the PSPC observation, only $\sim$ 170 seconds were taken in March 1991, the rest being taken in early May 1991.

Instrument	Exposure (s)	ROR #	P.I.	Start date
HRI	24613	rh6200021	Bregman	25 03 1991
PSPC	26088	rp600110	Watson	28 03 1991
HRI	9496	rh600021ao1	Bregman	20 10 1992

point sources removed. The particle contribution to the background was estimated using the master veto rate (Snowden et al. 1992) and the remainder was corrected for energy-dependent vignetting, to give a spatial-spectral model of the background covering the entire field. This model was then adjusted (by 3%) as a result of an iterative process of further source searching using the PSS programme (Allan 1995), removal of sources from the background annulus, and rescaling of the background to achieve a drop to zero surface brightness away from M 82. The resulting background subtraction should be accurate to 2%.

2.2. HRI reduction

The HRI's resolution and relative insensitivity to diffuse emission, make it an ideal instrument for investigating point sources in the field, clarifying the PSPC analysis. The data were binned into an image of size $0.3^\circ \times 0.3^\circ$ centred on the 2.2μm nucleus, with a $3''$ pixel size to exploit the HRI's superior spatial resolution. Given the flatness of the HRI vignetting function within the region of interest, no vignetting correction was applied. Source searching is described below.

3. Point sources

3.1. Source searching in the presence of diffuse emission

For M 82, source searching must take into account the presence of a spatially variable high surface brightness diffuse background due to the wind. This affects both the PSPC and the HRI. Failure to incorporate this additional background leads to the detection of large number of low significance sources within the diffuse emission, whilst simply increasing the threshold significance leads to the non-detection of what are clearly real sources in regions free of diffuse emission.

As a result of this we employ an iterative procedure which starts by using a smoothed image (including all sources and diffuse emission) as the background for the source searching procedure. Sources detected at $\gtrsim 5\sigma$ are then excised from the image, out to the $\sim$ 80% enclosed energy radius ($7''$ in the HRI, $26''$ in the PSPC), and the resulting holes interpolated over. This dataset is then smoothed to provide a second approximation to the background. The 80% radius, to which sources are removed, is a compromise between removing so large a radius that the interpolation is unreliable, and too small a radius, leaving significant source contamination in the background. The above procedure of source searching followed by background estimation, was repeated until there was no further change in the list

Table 2. PSPC and HRI detected sources. Positional errors are at 90% confidence, flux errors are 1 σ. Where a source is detected both in the PSPC and the HRI the HRI determined position is given.

Source	RA (J2000.0)	Dec. (J2000.0)	Pos. Err. (arcmin)	Flux (PSPC) Counts	Flux (HRI) Counts	Identification
1	09 54 20	+69 46 42	0.10	41 ± 8		
2	09 54 34	+69 48 13	0.17	33 ± 8		
3	09 55 07	+69 43 40	0.11	40 ± 9		Wind enhancement?
4	09 55 15	+69 36 19	0.04	39 ± 8	17 ± 7	
5	09 55 16	+69 47 41	0.06	120 ± 13	45 ± 9	
6	09 55 33	+69 44 47	0.10	62 ± 12		Wind enhancement?
7	09 55 47	+69 41 28	0.03		48 ± 13	
8	09 55 51	+69 40 48	0.01	8398 ± 108	1195 ± 48	M 82 nuclear source
9	09 56 02	+69 41 13	0.02		49 ± 11	
10	09 56 18	+69 49 02	0.04		18 ± 6	
11	09 56 22	+69 38 53	0.04		15 ± 6	
12	09 56 43	+69 38 05	0.17	37 ± 9		Wind enhancement?
13	09 56 59	+69 38 52	0.04	35 ± 8	23 ± 7	QSO 0952+698
14	09 57 00	+69 34 21	0.11	57 ± 9		
15	09 57 13	+69 44 18	0.04		15 ± 6	
16	09 57 23	+69 35 36	0.03	67 ± 10	26 ± 8	

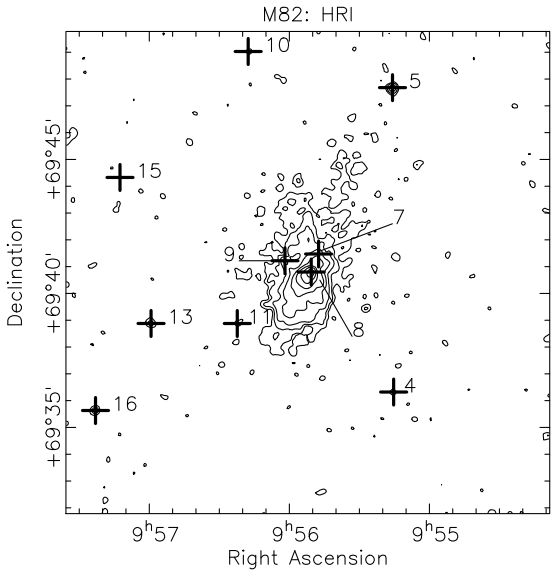

Fig. 2. Background subtracted HRI image of M 82. The data have been lightly smoothed with a Gaussian of $\sigma = 6''$. Contour levels begin at 4.0×10^{-3} counts s^{-1} arcmin^{-2}, an increase in factors of two. HRI sources detected as described in the text are marked by crosses, and are numbered as in Table 2.

of detected sources. In practice this required three cycles. The results of the method depend on the smoothing scale employed when estimating the background, and $\sigma = 18''$ and $60''$ were found to give best results for the HRI and PSPC, respectively. The final combined sourcelist is shown in Table 2.

3.2. Source spectra

Individual exposure-corrected spectra centred on the positions given in Table 2 were obtained for each PSPC source from the data cube within a radius corresponding to a 95% enclosed energy fraction at an energy of 0.5 keV (an appropriate energy for QSO's which form the majority of background sources). Raymond & Smith (1977) and power law models were fitted to these spectra. Standard χ^2 fitting is inappropriate, due to the low numbers of counts per bin; we therefore used a maximum-likelihood fit. For each source, the spectrum predicted from the spectral model is added to an estimated background spectrum derived from the background model cube discussed in Sect. 2.1. The resulting total source plus background spectrum is fitted to the observed spectral data using the Cash C-statistic (Cash 1979).

Table 3 gives the results of the spectral fits. As maximum likelihood does not provide a goodness-of-fit measure akin to χ^2, it is difficult to assess how good the fits are, except by visual inspection and comparing the fitted parameters with typical values for QSO's and stars. Source 8 (the nucleus) is strong enough that significant systematic discrepancies between the data and the fitted models are apparent, and is dealt with separately in Sect. 3.4.

3.3. Comparison between PSPC and HRI sources

Given the presence of several possible point sources within or in close proximity to the diffuse emission, the use of the HRI can clarify whether these are true point sources or not. As discussed in Sect. 2.2 the presence of strong diffuse emission complicates source searching, which may lead to the detection of spurious sources within the diffuse emission.

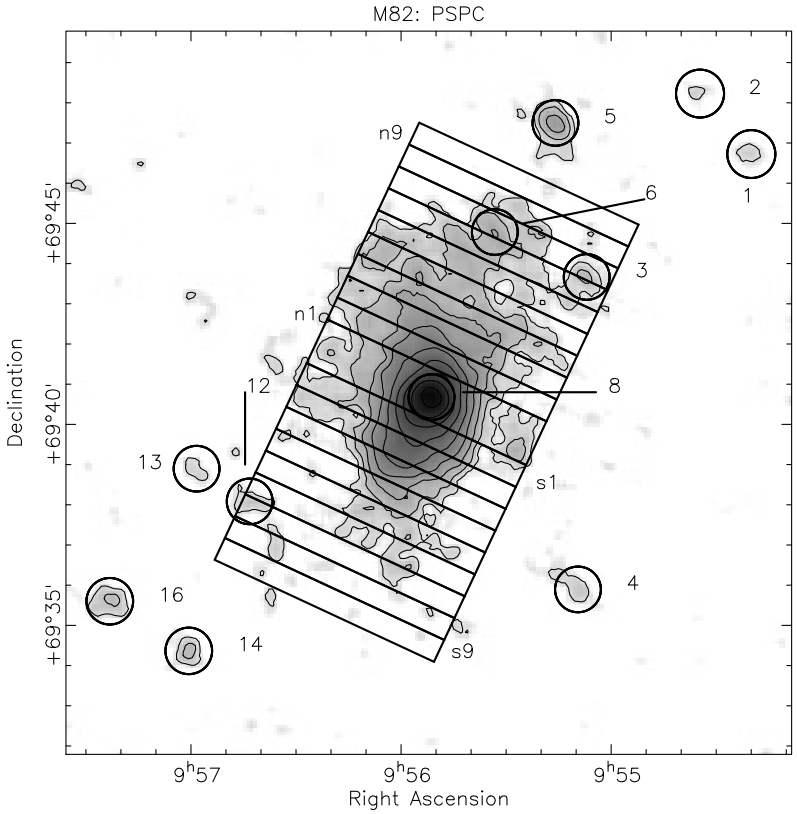

Fig. 3. The wind regions from which spectra were collected, overlaid onto an X-ray image. Sources (shown as circles and numbered as in Table 2) were removed from the analysis. Contour levels are as in Fig. 1.

Table 3. PSPC source properties. Error bounds are 1 σ. The best-fit parameters for a Raymond-Smith hot plasma model and a power law model are given.

Source	Raymond-Smith			Power Law		
	$N_{\rm H}$ (10^{21} cm^{-2})	T (keV)	EM (10^{55} cm^3 / 10 kpc^2)	$N_{\rm H}$ (10^{21} cm^{-2})	α	normalisation (10^{-5} photons cm^{-2} s^{-1} keV^{-1})
1	$0.28^{+0.28}_{-0.17}$	$1.78^{+20}_{-0.47}$	$5.4^{+5.7}_{-2.0}$	$0.48^{+0.44}_{-0.31}$	$2.3^{+1.0}_{-0.9}$	$0.8^{+0.2}_{-0.2}$
2	$0.35^{+0.73}_{-0.35}$	$0.88^{+1.32}_{-0.40}$	$4.9^{+9.8}_{-4.6}$	$0.70^{+1.16}_{-0.47}$	$2.7^{+1.3}_{-1.2}$	$0.7^{+0.4}_{-0.2}$
3	$4.2^{+7.6}_{-4.2}$	$0.23^{+0.36}_{-0.18}$	$48.7^{+26580}_{-48.7}$	$7.5^{+0.9}_{-2.5}$	8.0 ± 1.6	$12.4^{+4.6}_{-6.6}$
4	$0.00^{+0.06}_{-0.00}$	$0.57^{+0.18}_{-0.17}$	$2.0^{+1.7}_{-0.7}$	$(0.19^{+0.33}_{-0.19})$	(2.2 ± 1.0)	$(0.7^{+0.1}_{-0.2})$
5	$0.79^{+1.26}_{-0.28}$	$0.65^{+0.14}_{-0.34}$	$32.1^{+59.1}_{-16.1}$	$8.5^{+0.7}_{-3.2}$	8.0 ± 2.2	$31.7^{+5.4}_{-14.8}$
6	$0.87^{+0.30}_{-0.20}$	$0.36^{+0.08}_{-0.06}$	$100.3^{+97.8}_{-48.6}$	$1.77^{+0.79}_{-0.36}$	$4.6^{+0.7}_{-0.5}$	$48.0^{+12.4}_{-6.3}$
8	$(3.17^{+0.24}_{-0.17})$	$(2.39^{+0.48}_{-0.43})$	(3770^{+30}_{-20})	$3.96^{+0.29}_{-0.28}$	$2.17^{+0.14}_{-0.13}$	717^{+56}_{-44}
12	$0.9^{+3.4}_{-0.4}$	$0.43^{+0.24}_{-0.30}$	36^{+144}_{-29}	5^{+6}_{-1}	$6.3^{+4.2}_{-2.2}$	$4.3^{+8.8}_{-4.3}$
13	2^{+7}_{-2}	$0.7^{+3.5}_{-0.2}$	24^{+409}_{-24}	4^{+7}_{-4}	$3.6^{+3.7}_{-2.2}$	$2.8^{+10.9}_{-2.8}$
14	$0.10^{+0.10}_{-0.08}$	$1.4^{+3.6}_{-0.6}$	$6.1^{+4.4}_{-2.0}$	$0.21^{+0.21}_{-0.15}$	2.2 ± 0.7	0.8 ± 0.2
16	$0.24^{+0.18}_{-0.14}$	$2.9^{+21.2}_{-0.5}$	$9.0^{+4.6}_{-2.3}$	$0.32^{+0.28}_{-0.22}$	1.7 ± 0.7	$1.4^{+0.3}_{-0.2}$

Only five sources were detected independently in both the PSPC and the HRI. We have searched for counterparts to these objects at other wavelengths in the SIMBAD database. One (Source 8) is M 82's nuclear source, another (Source 13) a QSO. The other three do not have any counterparts.

For the remaining PSPC sources not detected in the HRI, we found 3σ upper limits for the HRI flux due to any point source within a region defined by the PSPC positional uncertainty. These, together with predicted HRI count rates from the spectral fits to the PSPC sources, are given in Table 4. There is little difference between the predicted fluxes for the power law and Raymond & Smith models. For the sources detected in both PSPC and HRI, the observed HRI count rates agree well with those predicted, except for the nucleus, which is discussed below. In most other cases the upper limits are greater than (i.e. consistent with) the predicted count rates. For the two possible sources within the northern wind, sources 3 & 6, the predicted count rates are higher than the HRI 3σ upper limits. This could

mean that these are not true point sources, merely bright lumps in the wind. Note, however, that source 6 appears to be significantly cooler than the temperature of the wind emission in region n7, where it is centred. Alternatively, the predicted count rate could be overestimating the flux, due to the addition of diffuse flux along with real source flux. Variability is another possible explanation for the HRI non-detection.

3.4. The nucleus

As the HRI observations have shown (Collura et al. 1994; Bregman et al. 1995), the nucleus of M 82 contains a very luminous, variable X-ray source, along with non-uniform diffuse emission. It is little surprise that the single component fits to the nuclear source in the PSPC data (source 8 in Table 2) are of poor quality. Given the large number of counts in the spectrum (11033 ± 249) we can use standard χ^2 fitting. The power law from Table 2 has a reduced χ^2 of 7 with 19 degrees of freedom. An additional problem is the finite radius of $34''$ within which the spectrum was extracted. Although the 95% enclosed energy radius at 0.5 keV is good for almost all sources, the brightness of the nucleus, coupled with its hardness, means that significant flux is scattered outside this radius. At energies above ~ 1.75 keV this radius only encloses $\sim 70\%$ of the flux. Given the large number of photons involved, this is likely to have a significant effect on any fit.

Fitting the data from within a larger ($r = 0.02^\circ$, giving $\sim 90\%$ enclosed energy at 1.75 keV, 17473 ± 415 counts) radius from the nucleus, we achieve a best-fit reduced χ^2 of 2.08 with 15 degrees of freedom (see Table 5) using a two component soft Raymond & Smith plus harder bremsstrahlung model. The fitted temperature of the hard component is outside *ROSAT*'s energy range, and so should only be interpreted as being being significantly hotter than 6.2 keV. The spectrum can also be fitted by a two component power law plus Raymond & Smith model, however the fit requires the power law to have a *lower* column than the hot plasma component. This is not physically sensible if the hard component represents nuclear emission, so we rejected this model in favour of the Raymond & Smith plus bremsstrahlung model.

The predicted HRI count rate for the hard bremsstrahlung component derived above is ~ 0.15 cts s^{-1}, compared to the observed value of ~ 0.05 cts s^{-1}. The thin, hot component of the wind is predicted to provide very little emission in the *ROSAT* band (Suchkov et al. 1994), and there are no other strong point sources seen by the HRI. Since the HRI source associated with the nucleus is known to be variable (Collura et al. 1994) by a factor of several within the HRI observations, the difference between PSPC and HRI fluxes is most likely due to such variability.

The first HRI observation (rh600021, see Table 1), is divided into two blocks which are interleaved with the PSPC observation. The short (~ 170 s) initial HRI pointing showed the source intensity at a level $\sim \frac{1}{3}$ that of the remaining HRI data, taken ~ 40 days later. The first block of PSPC data falls in this 40 day gap, with the remainder commencing ~ 200 days later.

Table 4. HRI count rates and upper limits for the PSPC detected sources. The predicted HRI count rate was calculated as described in the text. Only five PSPC sources are directly detected in the HRI, the remaining sources have 3σ upper limits quoted. The range in predicted flux corresponds to using either the power law or Raymond-Smith fit.

Source	Predicted flux (10^{-4} cts s^{-1})	Observed Flux (10^{-4} cts s^{-1})
1	5.9–6.3	< 9.5
2	4.9–5.4	< 9.4
3	12.8–13.4	< 10.2
4	6.1–6.9	6.6 ± 2.6
5	21.8–24.3	18.8 ± 3.8
6	25.8–29.5	< 12.5
8	1857–1996	500 ± 20
12	8.6–8.8	< 10.8
13	7.1–7.2	9.3 ± 3.0
14	7.9–8.0	< 9.7
16	10.9-11.3	11.0 ± 3.0

Table 5. Best-fit parameters (reduced $\chi^2 = 2.08$) for the nuclear source. Luminosities are quoted in the *ROSAT* band ($0.1 - 2.4$ keV), for a distance of 3.63 Mpc (Freedman et al. 1994) to M 82. The luminosity escaping M 82 L_{X-esc} is corrected for absorption in our own galaxy. The intrinsic source luminosities L_{X-in} are corrected to zero absorption. † This is the 1σ lower bound. The temperature is unbounded above this value.

Parameter	Hard component bremsstrahlung	Soft component Raymond & Smith
$N_{\rm H}$ (10^{21} cm^{-2})	$5.76^{+1.49}_{-1.17}$	$0.92^{+0.08}_{-0.12}$
EM (10^{57} cm^3/10 kpc^2)	$36.7^{+2.6}_{-3.4}$	$8.3^{+2.3}_{-2.5}$
T (keV)	$> 6.2^\dagger$	$0.76^{+0.02}_{-0.03}$
Metallicity ($Z_\odot$)	-	$0.30^{+0.09}_{-0.05}$
L_{X-esc} (erg s^{-1})	1.3×10^{40}	7.8×10^{39}
L_{X-in} (erg s^{-1})	3.5×10^{40}	1.2×10^{40}

We have searched for variation of the nuclear source within the PSPC observation, which is broken into three main blocks separated by long gaps, but observe no significant variation between the blocks. In the second HRI observation, taken a year later, the nuclear count rate decreases steadily over a period of six days from the previous HRI level to about half that (Collura et al. 1994).

The intrinsic nuclear point source luminosity in the *ROSAT* band of $\sim 3.5 \times 10^{40}$ erg s^{-1} (Table 5) is significantly higher than the *ROSAT* HRI estimate of $\sim 6.3 \times 10^{39}$ erg s^{-1}. This estimate assumed a Raymond-Smith model with $T = 3$ keV and $\log N_{\rm H} = 21.5$. With the higher temperature and absorption column inferred from the PSPC spectral fit, the HRI luminosity would increase, although the inferred PSPC luminosity remains several times higher. This PSPC luminosity corresponds to the

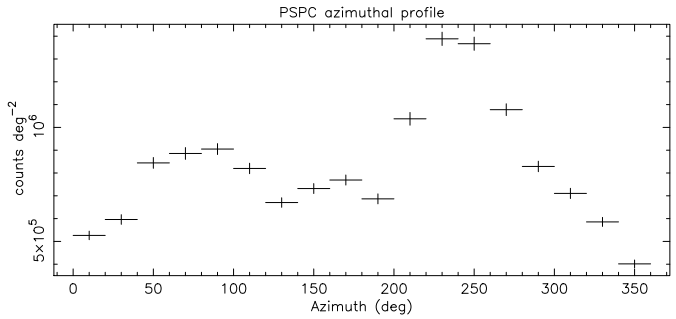

Fig. 4. Azimuthal profile of the emission within 0.1° of the nuclear source. Sources other than the nucleus have been masked out. The northern minor axis is at an azimuth of 65°, the southern minor axis at 245°.

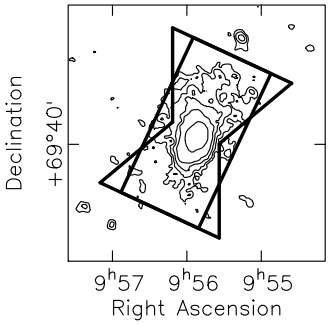

Fig. 5. Cylindrical and conical geometries assumed for the spectral analysis.

Eddington luminosity for a $\sim 250\,M_\odot$ object. The position of this source corresponds (to within *ROSAT* pointing accuracy) to the position of a strong 6 cm radio source (41.5+597) which, on the basis of a 100% drop in flux within a year, is unlikely to be a supernova remnant (Muxlow et al. 1994). A high surface brightness complex is seen in the optical (region E in O'Connell et al. 1995) at this position. This is an unusual object deserving more study.

4. Wind properties

4.1. Analysing the wind

As our aim is to derive spatially resolved plasma parameters (temperature, density, metallicity and absorbing column) it is necessary to assume a geometry for the emission. This will dictate the regions from which spectra are taken and the volumes used in deriving the density of the emitting plasma. Given the lack of symmetry of the diffuse emission (henceforth called the wind, bearing in mind alternative explanations of its origin as wind-shocked ambient material or even a hydrostatic halo as discussed in Sect. 5) apparent in Fig. 1, it is not obvious what geometry to choose. Within the wind paradigm, a conical (e.g. Suchkov et al. 1994) to cylindrical outflow (e.g. Tomisaka & Ikeuchi 1988; Tomisaka & Bregman 1993) along the galaxy's minor axis is expected, and if the emission arises from wind-shocked material a similar geometry would apply.

The azimuthal profile (Fig. 4) of the PSPC data about the centre of the galaxy can be used to explore the geometry of the diffuse emission. A biconical outflow would result in a sharp drop in the azimuthal brightness profile at the angles corresponding to the edges of the cone. If the cone were actually limb brightened (as suggested in some models), then a bimodal structure would be seen in the azimuthal profile of each outflow. In practice, the profile varies quite smoothly with azimuth in both hemispheres, and no suggestion of a limb brightening is apparent. It appears that a conical geometry is a poor representation.

Inspection of the surface brightness shows the Northern wind to be reasonably well described as a cylinder of radius $r = 0.05^\circ$. We therefore adopt a cylindrical geometry for the bulk of our analysis. For consistency, we apply the same geometry to the southern wind, although it is clear from Fig. 3 that this is a poorer approximation, which will overestimate the emitting volume.

A set of spectra along the northern and southern winds were accordingly extracted from a series of rectangular regions of width 0.1° and height h along the minor axis (Fig. 3). A compromise must be made between large h (collecting a larger number of photons in the spectrum) and small h (giving good spatial resolution along the wind). A value of $h = 0.01^\circ$ was chosen, giving 9 regions along the wind while still having sufficient photons to give reasonable constraints on the spectra for all but the outermost regions. Corresponding background spectra were formed from the background-model cube for each of the wind region to allow maximum likelihood fitting.

Since it is likely that there will in practice be some degree of divergence of the outflows (though as we will show, the X-ray emission is almost certainly not coming from the wind fluid itself), we have investigated the effects of this by performing an identical analysis using two truncated cones. These truncated cones have a radius in the galactic plane $r_{\rm base} = 0.03^\circ$, and an opening angle of 50°. The height h is again 0.01°. The cylindrical and diverging geometries are compared in Fig. 5.

As discussed in Sect. 3.3, several point-sources were detected within or in close proximity to the diffuse wind emission. While it is possible that these represent regions of enhanced diffuse emission rather than truly independent sources, they were masked out of the wind regions to prevent any possible contamination of the wind spectra by foreign flux. The spectra were then corrected for dead-time and exposure corrected.

Raymond & Smith (1977) hot-plasma models were then fitted to the strip spectra using maximum likelihood, initially allowing all parameters to optimise. It was found that the metallicities consistently fitted low, 0.00–$0.07 Z_\odot$. In view of the present uncertainties in the accuracy of *ROSAT* metallicities (see Bauer & Bregman 1996), and the expectation that the metallicity should not vary greatly through the wind, we refitted all the spectra with the metal abundance fixed at $0.05 Z_\odot$, which reduced the scatter in the other fit parameters. All results for the wind quoted below are derived from these $Z = 0.05 Z_\odot$ fits.

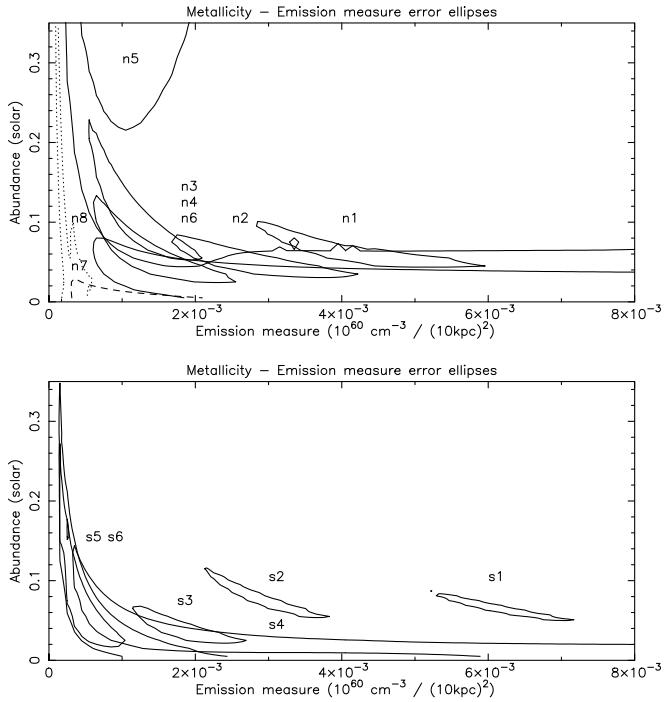

Fig. 6. Error ellipses for metallicity against emission measure at 68% confidence for two interesting parameters, for all the wind regions. Regions n7 and n8 are clearly peculiar as discussed in Sect. 4.5. Region n5 is poorly constrained.

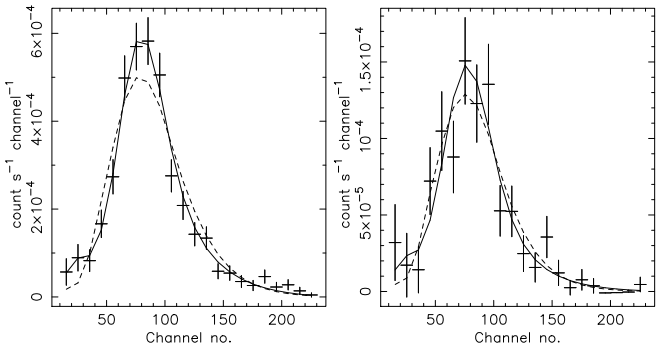

Fig. 7. Spectral fits to two for two of the wind regions, n2 (left) and n6 (right), representative of the range in quality of the spectra obtained. Normalised background-subtracted spectra are shown overlaid with power law (dashed line) and contamination corrected Raymond & Smith (solid line) best fits. For the inner regions (such as n2) the power law is clearly a poorer fit than the Raymond & Smith model.

Such a low metallicity, whilst surprising, is supported by the results of recent ASCA observations (Ptak et al. 1996; Tsuru 1996). ASCA has the spectral resolution to clearly distinguish the iron L complex, which is the strongest metallicity indicator for plasmas of this temperature, and the implied iron abundances in the soft spectral component is 0.04–0.05 $Z_\odot$ (with a typical error of ≈ 0.02), in good agreement with our results.

Since emission lines are so strong in the *ROSAT* energy band for $T \sim 0.5$ keV plasma, metallicity trades off against emission measure in fitted spectra. This can be clearly seen in Fig. 6, which shows the error ellipses for 68% confidence for *two* interesting parameters (optimising temperature and absorbing column) for all of the regions used in the analysis. Hence any error in our assumed metallicity will lead to a corresponding error in derived emission measure, and hence in inferred gas density. As can be seen, from Fig. 6, the error envelopes generally fall below $Z = 0.2Z_\odot$. Hence, taking $Z = 0.2Z_\odot$ as the highest plausible value for metallicity (though this falls well outside the ASCA errors), our emission measures would be overestimated by a factor ~ 4, and hence the densities would be a factor ~ 2 too high. Such an error is quite modest compared to those introduced by the unknown filling factor and uncertain geometry of the emitting material.

As previous X-ray observations of M 82 have been unable to determine whether a hot plasma or a power law gives a better fit, we also fitted power law spectra to the data. These were found to give significantly poorer fits than the hot plasma fits (see e.g. Fig. 7) for all but the outer regions, where the statistics were too poor to tell. Although maximum likelihood gives no absolute goodness of fit measure, the relative likelihood between two fits to the same data can be derived from the Cash C-statistic. From Cash (1979), the relative probabilities $P_2/P_1 = \exp(\Delta C_{12}/2)$, where $\Delta C_{12} = C_1 - C_2$ is the change in Cash statistic between the two fits. For the inner wind, contamination-corrected Raymond & Smith fits are clearly superior, e.g. for region n2, the hot plasma fit is ~ 400 times more probable than the best-fit power law.

4.2. Nuclear contamination of the wind

Given the presence of an extremely luminous hard point source (nearly a third of all counts detected from M 82 with the PSPC are within a PSF sized region of $r \sim 30''$) at the centre of M 82, and the increasing size of the PSPC PSF at higher energies, one expects some contamination of the wind emission in the inner strips by photons from the nuclear source.

We can roughly assess the level of contamination by asking what fraction of the flux within the two innermost wind regions (n1 and s1) is due to scattered nuclear flux. If we assume all the flux within a $r = 0.02^\circ$ region centred on the nuclear source were due to a point source, then the fraction of this flux scattered into wind region n1 is 15% of the total flux observed in n1. For the innermost southern region, s1, the value is 12%. These are overestimates, as only $\sim \frac{1}{2}$ of the flux within $r = 0.02^\circ$ is due to the point source.

We allow for nuclear contamination by using two-component models for the wind regions: a soft Raymond & Smith plasma for the wind, and a harder bremsstrahlung component for the nuclear contamination. The bremsstrahlung component in each strip was fixed: the absorbing column and temperature taking the values derived from the nuclear fit discussed in Sect. 3.4, and the contaminating flux being estimated from the (energy dependent) PSPC point spread function.

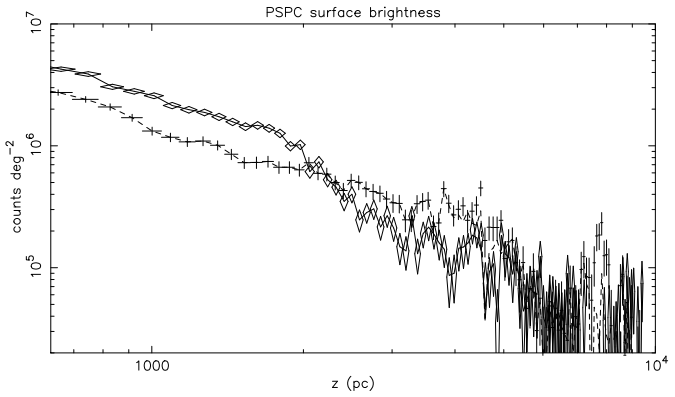

Fig. 8. Surface brightness along the minor axis in a slice 0.1° wide. Diamonds represent the emission to the south, crosses the northern data. In each case the line represents the data with sources (other than the nuclear source) excluded. The south is brighter than the north within $\sim$ 2 kpc in both the X-ray and the radio (Seaquist & Odegard 1991). Diffuse emission extends out to $\sim$ 6 kpc. The emission seen in the north at $z \sim 7.5$ kpc is a point source (number 5 in Fig. 3).

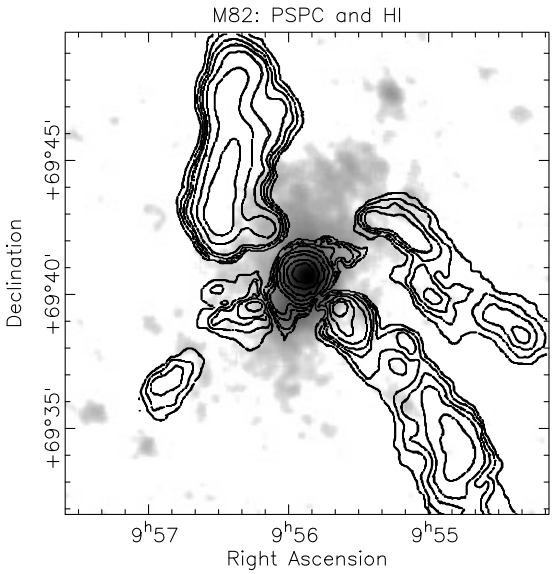

Fig. 9. Comparison between X-ray and HI distributions. A greyscale X-ray image (lowest tone corresponding a flux of 1.44×10^{-3}counts s^{-1} arcmin^{-2}), overlaid with contours of HI column density (adapted from Yun et al. (1993)). The contours correspond to 2.7×10^{19} cm^{-2} times 1, 2, 3, 4, 6, 10, 15 and 25.

4.3. X-ray morphology

It is clear from Fig. 1 that the diffuse emission is not symmetric around the plane of the galaxy. The surface brightness in a strip of width 0.10° parallel to the minor axis (Fig. 8) is initially higher to the south, but then drops more rapidly than to the north. Beyond 2 kpc ($\sim 120''$) from the nucleus the northern wind is consistently brighter. This asymmetry is also seen in the radio data of Seaquist & Odegard (1991). Within $100''$ of the nucleus, the brightness profile at 20 cm is brighter towards the south, while beyond $100''$ the north is brighter.

Emission can be traced out to $z \approx 0.1^\circ$ ($\equiv$ 6 kpc) from the nucleus along the minor axis, before dropping into the noise. The *Einstein* IPC estimate of emission extending to $\sim 9'$ from the nucleus was due to the inclusion of a point source (source 5 in Table 2) in the diffuse emission (see Fig. 3 in Fabbiano 1988).

4.4. Comparison with HI distribution

As can be seen in Fig. 9, the X-ray emission appears to anti-correlate with the large scale distribution of HI surrounding M 82. To the north-east, the X-ray emission appears to be bounded by the northern tidal streamer. Yun et al. (1993) claim this to be M 82's tidally disrupted outer HI disk. To the north-west, another streamer of HI intrudes onto the X-ray distribution on the eastern edge of regions n4 and n5. This northern HI has a velocity consistent with being on the far side of M 82, as is the northern wind. The southern wind appears confined between the clump of hydrogen to the south-east and the beginnings of the southern tidal streamer to the south-west. The south-eastern HI clump shows a broad blueshifted line wing which Yun et al. (1993) note may be due to the impact of a wind. The HI in the tidal streamers could provide a natural obstacle for the wind, constraining its expansion. The northern and southern streamers each contain $\sim 6 \times 10^7\, M_\odot$, similar to the mass of material we infer below for the soft X-ray emitting material in the wind; so the HI could potentially form a significant barrier for the wind.

In the inner regions, Fig. 9, shows significant amounts of HI in the region occupied by the optical filamentation and inner wind. The inner HI displays a velocity gradient along the minor axis in the same sense as the Hα emission, hence the HI probably consists of material swept out of the disk by the wind. As is discussed below, the X-ray spectra show signs of excess absorption.

4.5. Wind parameters

The results of the spectral fitting to the wind regions are given in Table 6. Contamination of the spectral properties of the wind by the nuclear point source has been allowed for as discussed in Sect. 4.2. As can be seen from Fig. 3 there is little wind emission beyond regions n8 and s6, and no useful spectral parameters could be derived for these outermost strips.

The absorbing column is found to decrease as the distance from the plane of the galaxy increases. Only in the south does the column drop to the Stark (1992) value of $4.0 \pm 0.5 \times 10^{20}$ cm^{-2}. It can be seen from Fig. 9 that, on the basis of the HI distribution, excess $N_{\rm H}$ would be expected to extend only to $z \sim 2$ kpc, and the magnitude of the observed excess for the north ($\sim 3 \times 10^{20}$ cm^{-2}) is larger than expected, except in the nuclear region. Absorption in the ROSAT band arises predominantly from He, C, N, and O rather than HI, hence, if the absorbing gas has a low metallicity such as is inferred for the hot X-ray emitting gas, the absorbing masses required at large heights above the plane are several 10^7 to several $10^8 M_\odot$.

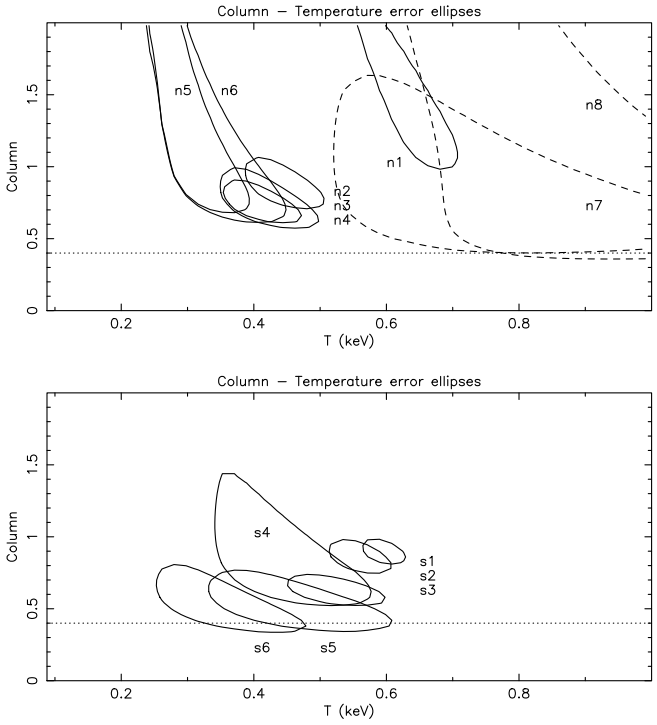

Fig. 10a and b. Error ellipses for column against temperature at 68% confidence in two interesting parameters for the wind regions. Regions n7 and n8 are peculiar, as discussed in Sect. 4.5. The dotted line shows the Stark column. For the northern regions (n1-n6) it is clear that: **a** (upper figure) altering the temperature will not remove the need for excess absorption, and **b** (lower figure) the temperatures for the innermost regions are well determined.

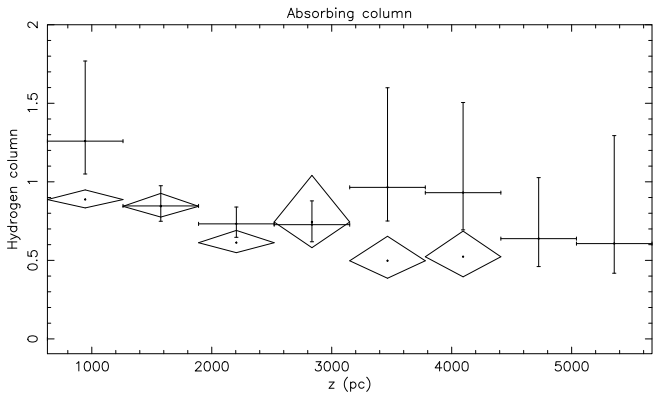

Fig. 11. Absorbing column against minor axis distance for Northern (crosses) and Southern (diamonds) winds. The column is in units of 10^{21} cm^{-2} . The Stark (1992) column is 0.40 ± 0.05 in these units. As the northern side of M 82 is inclined away from us, the initially higher column to the north is entirely natural.

Fig. 10 shows 68% confidence error ellipses for column and temperature. Excess absorption is required to the north, although the column for the south drops to close to the Stark value. The temperatures are well constrained, and do not depend strongly on the fitted column. The origin of the excess absorption to the north remains to be determined.

Temperature and density both decrease with increasing distance along the minor axis z, although the temperature drop is small (Figs 12 – 13). The density is initially higher to the south, but then drops below the density to the north beyond ~ 2 kpc, as indicated by the surface brightness profiles (Fig. 8).

Under our assumed cylindrical geometry, it is possible to derive further useful gas parameters (see Table 7). We assume a distance of 3.63 Mpc to M 82 throughout. The volume V is derived from the geometry, of which the emitting gas is assumed to occupy some fraction η (the filling factor of the hot gas). The fitted emission measure then equals $\eta\, n_e^2\, V$, and (assuming an ionised hydrogen plasma for simplicity) the mean electron density, total gas mass $M_{\rm gas} = m_{\rm H}\, n_e\, V$, thermal energy $E_{\rm th} = 3\, n_e\, V\, {\rm k}T$, bulk kinetic energy $K_{\rm gas} = \frac{1}{2}\, M_{\rm gas} v_{\rm gas}^2$, cooling timescale $t_{\rm cool} = E_{\rm th}/L_{\rm X}$, mass deposition rate $\dot{M}_{\rm cool} = M_{\rm gas}/t_{\rm cool}$, and sound speed $C_{\rm sound} = \sqrt{(2\,\gamma\,{\rm k}\,T\,/m_{\rm H})}$, can then be calculated. The intrinsic (i.e. corrected for both galactic and intrinsic absorption) X-ray luminosity L_{X-in} in the *ROSAT* band is also given.

In order to quantify the trends in the data, particularly in the behaviour of the temperature and density with increasing distance along the wind, we perform weighted least-squares fits to the data for north and south separately. We also regress temperature against density using weighted orthogonal regression (Feigelson & Babu 1992), allowing for the significant errors on both axes, using the package ODRPACK (Boggs et al. 1992).

Table 8 gives the fitted slopes, while the data and fitted lines are plotted in Figs. 12 - 14. The fits used data for regions n1-n6 and s1-s6 only; regions n7 & n8 were excluded as they clearly deviate from the general trend in the North.

The elevated temperatures of n7 and n8 are difficult to explain. We have checked that the two point sources which fall in the vicinity have been effectively excluded from the data. One obvious possibility is that the temperature rise is due to a shock, however, in this case the density would also be expected to rise, whereas it appears *lower* than expected from the trend of the inner six northern regions. A hardness map shows a lack of soft flux at the edges of the wind in regions n7 and n8, with no corresponding lack of hard flux, but the regions of reduced soft flux do not seem to correspond to areas of excess HI and hence higher absorption. We have investigated the possibility of the excess hard flux being due to the energy dependent scattering from inner regions of the wind, but such contamination from one region into the next is at too low a level, *decreases* in importance with z, and is not strongly energy dependent. Also, it should be noted that there is no corresponding temperature rise in the south.

A systematic error in the background subtraction could possibly mimic a real trend with increasing distance along the wind due to the increasing importance of the background as the surface brightness of the emission decreases. To check the effects of this, the analysis was repeated for backgrounds 5% over and undersubtracted with respect to the ideal background described

Table 6. Spectral fits to the wind regions. The Stark column is $0.40 \pm 0.05 \times 10^{21}$ cm^{-2} . The metallicity is frozen at $0.05 Z_{\odot}$.

Region	Counts	Raymond-Smith parameters		
		$N_{\rm H}$ (10^{21} cm^{-2})	T (keV)	EM (10^{56} cm^3 / 10 kpc^2)
n1	1714 ± 43	$1.26^{+0.51}_{-0.21}$	$0.65^{+0.04}_{-0.06}$	$44.7^{+10.2}_{-3.6}$
n2	810 ± 30	$0.85^{+0.13}_{-0.10}$	$0.44^{+0.04}_{-0.04}$	$26.0^{+4.7}_{-3.5}$
n3	579 ± 26	$0.73^{+0.11}_{-0.09}$	$0.41^{+0.04}_{-0.04}$	$20.0^{+3.9}_{-3.1}$
n4	416 ± 23	$0.73^{+0.15}_{-0.11}$	$0.41^{+0.05}_{-0.05}$	$13.9^{+3.5}_{-2.6}$
n5	295 ± 20	$0.96^{+0.63}_{-0.21}$	$0.32^{+0.05}_{-0.12}$	$16.3^{+10.4}_{-4.3}$
n6	198 ± 17	$0.94^{+0.57}_{-0.24}$	$0.33^{+0.07}_{-0.07}$	$9.9^{+6.5}_{-3.2}$
n7	116 ± 14	$0.64^{+0.39}_{-0.18}$	$0.76^{+0.20}_{-0.15}$	$2.4^{+0.4}_{-0.3}$
n8	107 ± 14	$0.61^{+0.69}_{-0.19}$	$0.89^{+0.27}_{-0.14}$	$2.3^{+0.4}_{-0.3}$
n9	40 ± 12	–	–	–
s1	2859 ± 54	$0.89^{+0.06}_{-0.05}$	$0.60^{+0.02}_{-0.02}$	$69.6^{+3.3}_{-2.9}$
s2	1494 ± 40	$0.84^{+0.08}_{-0.07}$	$0.56^{+0.03}_{-0.03}$	$38.5^{+2.9}_{-2.5}$
s3	621 ± 27	$0.61^{+0.08}_{-0.06}$	$0.52^{+0.05}_{-0.05}$	$14.7^{+2.1}_{-1.5}$
s4	246 ± 19	$0.74^{+0.30}_{-0.16}$	$0.44^{+0.09}_{-0.07}$	$7.6^{+3.1}_{-1.8}$
s5	185 ± 17	$0.50^{+0.16}_{-0.11}$	$0.45^{+0.11}_{-0.08}$	$4.6^{+1.9}_{-1.1}$
s6	141 ± 16	$0.52^{+0.16}_{-0.13}$	$0.33^{+0.09}_{-0.06}$	$5.3^{+2.4}_{-1.8}$
s7	115 ± 15	–	–	–
s8	86 ± 14	–	–	–
s9	62 ± 13	–	–	–

Table 7. Derived gas parameters for the wind, assuming a distance of 3.63 Mpc to M 82. η is the volume filling factor of the gas. All parameters have been derived assuming η = 1. Conversion factors to arbitrary η are given. v_{1000} is the outflow velocity of the X-ray emitting gas in units of 1000 km s^{-1} , which may not be the same as the wind velocity.

Region	Volume (10^{65} cm^3)	$n_{\rm e}$ (10^{-3} cm^{-3}) ($\times 1/\sqrt{\eta}$)	$M_{\rm gas}$ ($10^6 M_{\odot}$) ($\times\sqrt{\eta}$)	$E_{\rm th}$ (10^{55} ergs) ($\times\sqrt{\eta}$)	$C_{\rm sound}$ km s^{-1}	$K_{\rm gas}$ (10^{55} ergs) ($v_{1000}^2 \times \sqrt{\eta}$)	$L_{\rm X-in}$ (10^{38} erg s^{-1}) (0.1 – 2.4 keV)	$t_{\rm cool}$ (Myr) ($\times\sqrt{\eta}$)	$\dot{M}_{\rm cool}$ ($M_{\odot} yr^{-1}$)
n1	5.85	$31.7^{+3.6}_{-1.4}$	15.4	5.6	460	15.4	33.8	520	0.030
n2	5.85	$24.2^{+2.2}_{-1.6}$	11.8	2.9	370	11.8	16.2	560	0.021
n3	5.85	$21.2^{+2.1}_{-1.7}$	10.4	2.4	360	10.4	11.8	640	0.016
n4	5.85	$17.7^{+2.2}_{-1.6}$	8.6	2.0	360	8.6	8.3	750	0.011
n5	5.85	$19.2^{+6.1}_{-2.5}$	9.4	1.7	320	9.4	8.3	640	0.015
n6	4.17	$17.7^{+5.8}_{-2.9}$	6.2	1.1	330	6.2	5.2	690	0.009
n7	4.15	$8.7^{+0.7}_{-0.5}$	3.0	1.3	490	3.0	1.9	2160	0.001
n8	5.85	$7.1^{+0.6}_{-0.4}$	3.5	1.7	540	3.5	1.8	3050	0.001
Sub-total (North)			68.4	18.6		68.4	87.2		0.104
s1	5.85	$39.6^{+0.9}_{-0.8}$	19.3	6.4	440	19.3	51.0	400	0.048
s2	5.85	$29.4^{+1.1}_{-0.9}$	14.4	4.5	430	14.4	27.5	520	0.028
s3	5.85	$18.2^{+1.3}_{-0.9}$	8.9	2.6	410	8.9	10.1	800	0.011
s4	5.85	$13.0^{+2.7}_{-1.6}$	6.4	1.6	370	6.4	4.7	1050	0.006
s5	5.85	$10.1^{+2.1}_{-1.3}$	5.0	1.2	380	5.0	2.9	1370	0.004
s6	4.55	$10.9^{+2.5}_{-1.9}$	4.1	0.8	330	4.1	2.7	880	0.005
Sub-total (South)			58.1	17.0		58.1	98.9		0.102
Total			126.4	35.6		126.4	186.2		0.206

Table 8. Results of the linear regression applied separately to the data from both north and south winds as described in the text. z is the distance along the minor axis. Results are given for both the contamination "corrected" and uncorrected data to demonstrate the effect the contamination has. To assess the effect of the chosen geometry, results for a truncated conical geometry with radius on the major axis $r_{\rm base} = 0.03^\circ$ and an opening angle of 50° are also shown.

Cylinder, radius $r = 0.05^\circ$ Corrected for nuclear contamination of the wind.					
Relationship	Wind	Slope		Intercept	
			95% confidence interval		95% confidence interval
T:n_e	North	1.047 ± 0.206	0.474 to 1.620	1.374 ± 0.335	0.445 to 2.303
	South	0.262 ± 0.058	0.100 to 0.423	0.146 ± 0.087	-0.097 to 0.389
T:z	North	-0.474 ± 0.078	-0.691 to -0.258	1.208 ± 0.251	0.511 to 1.906
	South	-0.227 ± 0.060	-0.394 to -0.061	0.458 ± 0.186	0.057 to 0.974
n_e:z	North	-0.467 ± 0.045	-0.590 to -0.343	0.117 ± 0.144	-0.517 to 0.283
	South	-0.836 ± 0.108	-1.137 to -0.535	1.095 ± 0.334	0.168 to 2.022
Cylinder, radius $r = 0.05^\circ$. No contamination correction.					
Relationship	Wind	Slope		Intercept	
			95% confidence interval		95% confidence interval
T:n_e	North	0.821 ± 0.119	0.490 to 1.151	1.074 ± 0.195	0.532 to 1.616
	South	0.185 ± 0.052	0.041 to 0.329	0.079 ± 0.078	-0.137 to 0.295
T:z	North	-0.467 ± 0.058	-0.628 to -0.305	1.236 ± 0.188	0.715 to 1.758
	South	-0.188 ± 0.039	-0.295 to -0.081	0.384 ± 0.120	-0.052 to 0.715
n_e:z	North	-0.568 ± 0.072	-0.769 to -0.368	-0.189 ± 0.233	-0.457 to 0.835
	South	-0.922 ± 0.114	-1.239 to -0.606	1.353 ± 0.351	0.378 to 2.328
Truncated cone, radius $r_{\rm base} = 0.03^\circ$, opening angle $\theta_{\rm op} = 50^\circ$, contamination corrected.					
Relationship	Wind	Slope		Intercept	
			95% confidence interval		95% confidence interval
T:n_e	North	0.641 ± 0.135	0.266 to 1.0170	0.695 ± 0.207	0.121 to 1.270
	South	0.204 ± 0.051	0.063 to 0.346	0.037 ± 0.072	-0.164 to 0.237
T:z	North	-0.476 ± 0.089	-0.724 to -0.227	1.223 ± 0.284	0.436 to 2.010
	South	-0.228 ± 0.068	-0.418 to -0.038	0.459 ± 0.213	-0.132 to 1.049
n_e:z	North	-0.762 ± 0.027	-0.837 to -0.687	0.887 ± 0.086	0.649 to 1.125
	South	-1.103 ± 0.118	-1.431 to -0.775	2.023 ± 0.365	1.010 to 3.036

above. The fitted parameters were within 1σ of those from the standard background in all cases. Hence over or undersubtraction is not a serious problem.

4.6. The effect of the assumed geometry

As discussed in Sect. 4.1, M 82's X-ray emission is not obviously well approximated by either a conical or a cylindrical outflow. In addition, the asymmetry between north and south makes the choice of a consistent geometry difficult. The inclination of the galactic plane to our line of sight will also blur any results, by superposition of physically differing regions, even if the plasma's properties do vary only with z. It is not unreasonable to expect variation perpendicular to the minor axis, leading to further superposition of different components along the line of sight. We checked for this by performing spectral fits for regions n3, n4, s3 & s4, binning the emission into eastern, central and western spectra. The resulting temperatures across the wind fell within 1σ of each other, indicating that cross-wind variations are not a major effect.

Let us suppose that the plasma properties vary not with z, but with radius from the galactic centre, as in a spherical or conical outflow. Our derived spectral properties, using a cylindrical geometry, will then differ from the true properties. For a conical distribution, the degree to which the fitted parameters deviate from the true parameters depends on the opening angle of the cone. The fitted parameters will be some flux-weighted average of the various components of different r that fall within a slice at constant z. The effect will be worst for the inner regions, and for large cone opening angle, but will be small at large z. For a parameter F that decreases with r, the fitted parameter F at some z will always be lower than the true value for $r = z$, due to the incorporation of flux from regions of greater r and hence lower F. This will have the effect of flattening the slope of any

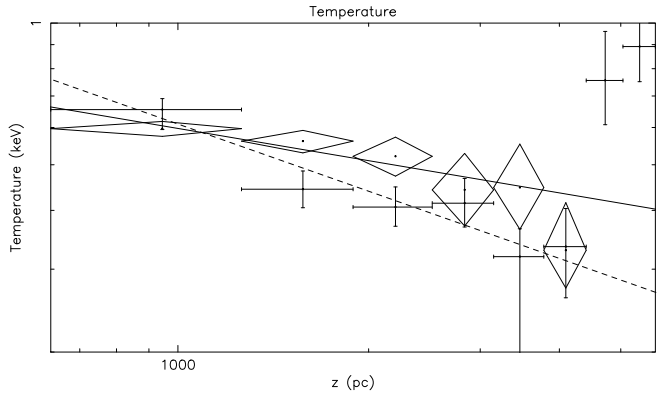

Fig. 12. Temperature against minor axis distance for Northern (data: crosses, regression line: dashed) and Southern(data: diamonds, regression line: solid) winds. Only the first six points (n1 – n6 and s1 – s6) are used in the regressions.

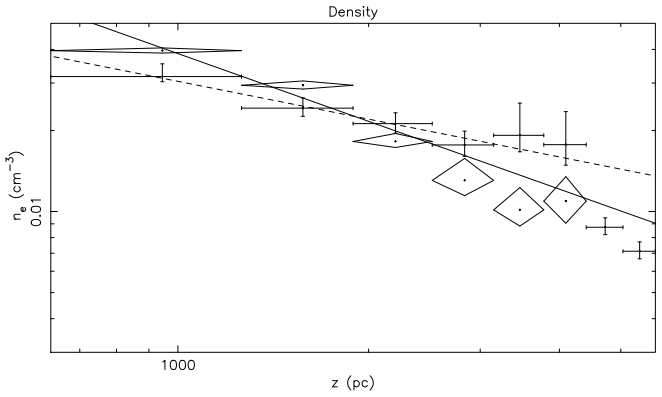

Fig. 13. Derived density against minor axis distance for Northern (data: crosses, regression line: dashed) and Southern (data: diamonds, regression line: solid) winds. Only the first six points (n1 – n6 and s1 – s6) are used in the regressions.

real trend in the data as the discrepancy between true and fitted values is less at large r.

In the present case, given the flatness of the temperature profile, the true temperature will not vary much from the fitted values. The emission measure will not be too far out either, given that the higher surface brightness emission along the minor axis dominates the fitted emission measure (i.e. the inclusion of the lower surface brightness emission further from the minor axis in our cylindrical geometry has rather little effect). The major source of bias is the volume, which we would overestimate at small r, and underestimate at large r. However, it should be borne in mind that the derived gas density depends only on the inverse square root of the assumed volume, $n_{\rm e} \propto \sqrt{({\rm EM}/V)}$.

In conclusion, if the soft X-ray emission does have a rather more divergent geometry than we have assumed, then the true temperatures will be similar to those obtained, while the density will drop off faster than our result, the inner densities being higher and the outer densities lower than those we have derived.

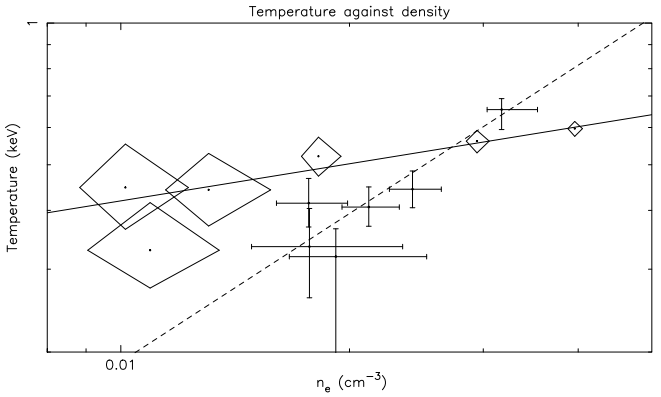

Fig. 14. Temperature against density for Northern (data: crosses, regression line: dashed) and Southern (data: diamonds, regression line: solid) winds. For an adiabatically expanding gas the slope of the $\log T : \log \rho$ regression line would be $\gamma - 1 = \frac{2}{3}$.

In order to test the magnitude of these effects, the standard analysis above was repeated treating the emission as arising from two inverted truncated cones of radius $r_0 = 0.03^\circ$ on the galactic major axis and semi-opening angle $\theta = 25^\circ$, chosen by eye to give an reasonable approximation to the observed emission in the North (see Fig. 5). The results of this on the derived trends in n and T, can be seen in Table 8. The slope of the $T : z$ relation is essentially unchanged, whilst the $n_{\rm e} : z$ trend becomes steeper, as expected. The implications of this will be discussed below.

5. Comparison with wind models

Given previous claims that the X-ray emission from M 82 is consistent with that expected from the adiabatic expansion of a free flowing wind (Fabbiano 1988; Bregman et al. 1995), in particular that the density derived from the surface brightness falls off as $\sim r^{-2}$, it is worth investigating whether our spectral results are consistent with this idea.

5.1. Chevalier & Clegg's adiabatic wind

The simplest useful model of a galactic wind is that of Chevalier & Clegg (1985). This is just a spherically-symmetric outflow from a region of constant mass and energy injection (the starburst) ignoring the effects of gravity, radiative cooling and the presence of any ambient medium. The hot gas smoothly passes through a sonic transition at the radius of the starburst region, and then becomes a supersonic outflow which cools adiabatically. Provided the kinetic energy supplied by the numerous SN and stellar winds within the starburst is efficiently thermalised, the temperature of the hot gas within the starburst region will be $\sim 10^8$ K for reasonable mass and energy injection rates, making the neglect of the effects of gravity and radiative cooling valid. For regions well outside the starburst region, $r \gg R_\star$, the wind density $\rho \propto r^{-2}$, wind temperature $T \propto r^{-4/3}$ and thermal pressure $P_{\rm th} \propto r^{-10/3}$. McCarthy et al. (1987) compared varia-

tion of pressure with radius in the optical filamentation with the Chevalier & Clegg (CC) model, under the assumption that the thermal pressure in the filaments would equal the total (thermal plus ram) pressure in the wind, achieving a good match within a kiloparsec of the nucleus. Fabbiano (1988) reported in a reanalysis of the *Einstein* IPC data, that the radial distribution of the X-ray emission was consistent with $\rho \propto r^{-2}$, i.e. a free-flowing wind.

The Chevalier & Clegg model assumes a spherical outflow, in contrast to the cylindrical geometry we have adopted. What would we expect to see from a free wind in a more generalised outflow geometry, e.g. a bubble that has broken out of the disk of the galaxy and now allows free escape of the wind material? Assuming a constant mass loss rate, $\dot{M} = \rho_r A_r v_r$, where A_r and v_r are the cross-sectional area and the velocity of the flow, and A_r of the form $A_r \propto r^{\beta}$, together with a constant outflow velocity, it follows that $\rho_r \propto r^{-\beta}$. For a cylinder, $\beta = 0$, hence ρ is constant. For a sphere or a cone of constant opening angle, $\beta = 2$. The density for a cone is just a constant ratio higher ($4\pi/\Omega$, where Ω is the opening angle in steradians) than that for a spherical wind for a constant $\dot{M}$. Obviously we can produce any ρ_r and retain the concept of the emission as arising from a free wind, by choosing the appropriate geometry. However, for isentropic gas, the temperature $T_r \propto \rho_r^{\gamma-1}$, where $\gamma = 5/3$ in the present case. In the absence of cooling (a good approximation given that the outflow timescale is $\sim 10^6 - 10^7$ yr while the cooling timescales are $\sim 10^9$ yr) a free wind would expand adiabatically. Hence we expect a $\log T : \log \rho$ graph to have a slope of $\gamma - 1 = \frac{2}{3}$ for *any* free wind irrespective of geometry. Inspection of Table 8 shows that although the northern emission is consistent with this, the southern emission is inconsistent at greater than the 95% confidence level, in the sense that the temperature drops too slowly relative to the density – i.e. the entropy *rises* outwards.

Note that if the absorbing columns in the northern outer regions are overestimated, then the real temperatures for these regions will be higher, reducing the temperature gradient. This would make the north less isentropic and reduce the difference between north and south. However the fits clearly require a higher column than Stark for these regions.

As discussed in Sect. 4.6, our use of a cylindrical geometry will lead us to underestimate the slope of the density profile if the emission comes from a conical outflow, whilst our temperature estimate is quite robust. This means that the inconsistency of the southern wind with an adiabatic outflow can only be *accentuated* if the flow diverges. The slopes for the re-analysis with a truncated conical geometry confirm this, the southern emission being less isentropic than for the cylindrical analysis.

Bearing in mind the geometry issue, we can attempt a more quantitative comparison between the observed temperatures and densities and the CC model, using the forms for ρ and T from CC, and the scaling relationships for the mass and energy injection given by Heckman et al. (1993). These use the predicted deposition of mass, kinetic energy and momentum from a starburst calculated by Leitherer et al. (1992). For a constant star formation rate over a period of 5×10^7 yr, solar metallicity and a normal Salpeter IMF extending up to $100\,M_\odot$, the various injection rates are related to the starburst bolometric luminosity by:

$$\dot{E} = 8 \times 10^{42}\, L_{\rm bol,11}\ {\rm erg\,s^{-1}} \quad (1)$$

$$\dot{M} = 3\, L_{\rm bol,11}\, M_\odot\ {\rm yr^{-1}} \quad (2)$$

where $L_{\rm bol,11}$ is the bolometric luminosity in units of $10^{11}\,L_\odot$. For most starbursts $L_{\rm FIR}$, is the dominant contributor to $L_{\rm bol}$ so it is a reasonable approximation to equate $L_{\rm bol,11}$ with $L_{\rm FIR}$. How valid are these scaling relations for M 82? Visual inspection of Leitherer et al.'s figures show that for all but the lowest metallicities the injection rates are approximately constant after $\sim 5 \times 10^6$ yr, similar to the age of M 82's starburst (Rieke et al., 1993).

Applying the above scaling relations to Chevalier & Clegg's model we obtain, for radii large compared to the starburst radius $R_\star$:

$$n_{\rm e}({\rm cm^{-3}}) = 8.14 \times 10^{-2} L_{\rm bol,11} \left(\frac{r}{R_\star}\right)^{-2} \left(\frac{4\pi}{\Omega}\right) \quad (3)$$

$$T({\rm keV}) = 4.13 \left(\frac{r}{R_\star}\right)^{-4/3} \left(\frac{4\pi}{\Omega}\right)^{2/3} \quad (4)$$

where $n_{\rm e}$ is the electron number density number density, T the temperature and Ω the total solid angle through which the wind flows out.

Note that the temperature is independent of $L_{\rm bol}$, being a ratio of the energy and mass injection rates. For a bolometric luminosity of $4 \times 10^{10}\,L_\odot$ (Rieke et al. 1993) and a characteristic radius, $R_\star$, for the starburst of 200 pc, we can predict ρ and T at radii corresponding to the regions in Fig. 3.2 – see Table 9. Even for the innermost regions (n1 and s1) the CC model underestimates the density by an order of magnitude. Although the predicted temperature is almost equal to that observed near the galactic centre, the adiabatically expanding wind cools too quickly to match the PSPC data, dropping to ~ 0.05 keV in the outermost regions, whereas the observed temperature along the minor axis is almost constant at $0.4 - 0.5$ keV and even rises in regions $n7$ and $n8$ to ~ 0.8 keV.

In summary, the densities and temperatures derived under our assumed cylindrical geometry differ greatly from those predicted under a spherical geometry by the CC model. Given an arbitrary outflow geometry, it is in principle possible for the adiabatic wind model to reproduce the observed shallower trend in density, however the departure of the southern wind from constant entropy is a robust result which is incompatible with the basic assumptions of the CC model. We conclude, therefore, that the observed X-ray emission cannot arise from a single phase, expanding wind. The fact that the entropy actually *rises* with z in the south, means that the CC model cannot be saved by supposing that additional material is entrained into the flow as it proceeds. Although this might raise the density, it would cause the entropy to decline with z, accentuating the disagreement with our results.

5.2. A hydrostatic halo

It has been suggested (W. Pietsch, private communication) that the extended X-ray emission around NGC 253 may be due not to a wind or shocked cloud emission, but to a static halo. For M 82 the optical emission line velocity data and spectral index variations in the radio halo (McKeith et al. 1995; Seaquist & Odegard 1991) demonstrate conclusively the presence of a galactic wind. Since the synchrotron emission is very similar to the X-ray in extent, so it is difficult to argue that the X-ray emission is not associated with a wind.

Can we rule out a hydrostatic halo on the basis of the observed X-ray properties? From the observed density and temperature the mass within some radius r for a hydrostatic halo, assuming spherical symmetry, is:

$$M(<r) \approx 4.45 \times 10^{10}\,(\beta+\epsilon)\,T_{\rm keV}\,r_{\rm kpc}\,M_{\odot}, \qquad (5)$$

where the observed temperature $T \propto r^{-\epsilon}$ and density $n_{\rm e} \propto r^{-\beta}$. For regions n3 and s3 the predicted mass within 2.2 kpc are $4 \times 10^{10}\,M_{\odot}$ and $5 \times 10^{10}\,M_{\odot}$ respectively. From Götz et al. (1990) the mass within this radius, based on velocities measured in HI , is $\sim 3 \times 10^{9}\,M_{\odot}$, an order of magnitude lower.

Hence we can rule out any possibility that the X-ray emitting gas is bound to M 82 as a static halo.

5.3. Shocked clouds in a wind

An alternative to emission from a free wind is emission from shocked material embedded in such a wind. Any clouds of denser material overrun by the wind, be they fragmented remnants of the dense shell swept up by the wind in its "snow-plough" phase or clouds in the ISM, will be shock-heated. The Hα filamentation seen along the minor axis has line ratios indicative of material shocked to $\sim 10^4$ K. Less dense material would be heated to even higher temperatures, and could be the source of the soft X-rays seen, rather than the emission being due to the wind itself.

The temperature to which these clouds will be heated depends on the speed of the shock driven into them by the wind. This depends on the relative densities of the cloud and the wind, and the wind velocity. In the case of strong shocks (Mach number M $\gg$ 1) we can ignore the thermal pressure of both the wind and the cloud, and equate momentum flux across the shock. Given the mass and energy injection rates, one expects a wind velocity $v_{\rm w} \approx 3000\,{\rm km\,s^{-1}}$, whereas the sound speed in the X-ray emitting gas is $\sim 400\,{\rm km\,s^{-1}}$. Clouds will be accelerated by the wind to varying extents depending on their column density and individual histories, but only to velocities of order hundreds of $\rm km\,s^{-1}$, as seen in the Hα filaments. Hence the strong shock approximation is not unreasonable. The shock driven into the cloud will then have a velocity $v_{\rm c} \approx v_{\rm w}\sqrt{\rho_{\rm w}/\rho_{\rm c}}$. The eventual temperature of the cloud will be proportional to $v_{\rm c}^2$.

Table 9. Predicted parameters of the X-ray emitting gas using the simple models discussed in Sect. 5. The shocked cloud temperatures are calculated using the derived electron densities from the northern wind for unit filling factor. Predicted cloud temperatures for the south are similar. Values assume spherical outflow for the wind. For a conical outflow of total solid angle Ω, the shocked cloud temperature $T_{\rm c}$ and the CC wind density are $\propto 4\pi/\Omega$, and the CC temperature $\propto (4\pi/\Omega)^{2/3}$.

Region	z	Chevalier & Clegg		Shocked clouds
		$n_{\rm e}$	$T_{\rm w}$	$T_{\rm c}$
	(pc)	($10^{-4}\,{\rm cm^{-3}}$)	(keV)	(keV)
1	945	14.6	0.52	1.58
2	1575	5.3	0.26	0.74
3	2205	2.7	0.17	0.43
4	2835	1.6	0.12	0.31
5	3465	1.1	0.09	0.19
6	4095	0.8	0.07	0.15
7	4725	0.6	0.06	0.23
8	5355	0.5	0.05	0.22

For a constant velocity, spherical or conical wind flowing into solid angle Ω, with constant mass injection rate $\dot{M}$, the wind density $\rho_{\rm w} \propto r^{-2}$, and the shocked cloud temperature

$$T_{\rm c} = 6.15 \times 10^{-3} v_{1000}\,\dot{M}\,r_{\rm kpc}^{-2}\,n_{\rm c}^{-1}\left(\frac{4\pi}{\Omega}\right)\ {\rm keV}, \qquad (6)$$

where v_{1000} is the wind velocity in units of $1000\,{\rm km\,s^{-1}}$, and $\dot{M}$ in units of $M_{\odot}\,{\rm yr^{-1}}$. We assume the postshock cloud density is four times the preshock density, and that ionization, dissociation, magnetic fields and radiative losses are negligible. Relaxing the previous four assumptions would result in lower shocked cloud temperatures.

Given $n_{\rm c} \approx 2n_{\rm e}$, the number densities derived above, a wind velocity of $3000\,{\rm km\,s^{-1}}$ and $\dot{M}$ from Eq. (2) we can predict the temperature we expect assuming unit filling factor and $\Omega = 4\pi$ (Table 9). From Fig. 1 one can estimate the solid angle the wind flows into as $\sim \pi$ steradians, raising $T_{\rm c}$ by a factor ~ 4. In the context of clouds in a wind, the filling factor should be substantially less than unity. The Hα filaments have $\eta \sim 10^{-2}$ (McCarthy et al. 1987) in the inner kiloparsec, so it would not be unreasonable to expect cloud filling factors of order $10^{-2}-10^{-1}$ at larger distances from the nucleus. This would reduce $T_{\rm c}$ by a factor $\sim$ 3–10. The net effect is that the predicted temperatures are rather lower than those observed, but considering the large uncertainties involved, this simple model must be regarded as giving results consistent with observation.

Assuming that Ω and the filling factor do not vary with distance along the wind, the predicted temperatures (Table 9) drop off too quickly to match the observed trend of T with z. The steepness of the predicted temperature profile could be due to the assumed geometry. As discussed in Sect. 4.6 the inner densities may be higher than calculated. Higher inner cloud densities would lead to lower postshock cloud temperatures and hence flatten the trend.

So, in summary, predicted postshock temperatures for a simple model where the wind shock heats clouds are consistent with, if slightly lower than, those observed, given the observed emission measure (density).

5.4. Numerical models

Tomisaka & Ikeuchi (1988) were the first to explicitly model the wind in M 82 using 2D hydrodynamical simulations. They found a roughly cylindrical bipolar wind formed naturally for a constant mass and energy input rate in the nucleus of 0.1 SN yr^{-1}. However, they modelled the ISM as a cold rotationally supported disk in which the angular velocity was independent of the distance from the plane of the disk. This physically unrealistic configuration creates a strong funnel along the z-axis which strongly collimates the wind. Tomisaka & Bregman (1993) allowed the rotational velocity to decrease exponentially away from the cold disk, into a hot low density halo. This distribution still provides a strong cylindrical funnel for the expansion of the wind at low z. Suchkov et al. (1994, hereafter SBHL) provide a more realistic ISM for their modelling of M 82: a two component cold rotating dense disk and non-rotating hot tenuous halo, and a starburst history incorporating the milder mass and energy input from stellar winds before the more energetic supernovae dominated stages. They find bipolar outflows form easily over a wide range in different halo and disk conditions. Shocked halo gas at temperatures $0.2 - 0.4$ keV provides the majority of the X-ray emission in their "soft" band ($0.1 - 2.2$ keV).

The eventual wind geometry depends on the initial gas distribution and the mass and energy input history. For those models with "mild" early winds (models A1 and A2 in SBHL) biconical outflows of opening angle $\theta \sim 60 - 90^\circ$ with dense disk material entrained along the surface do occur naturally. Initially the mild wind creates a cavity in the disk to the halo for the wind to escape, without substantially damaging the disk. The wind then propagates outward in the halo, sweeping it up and shocking it. In the later SN-driven stage of the starburst, the more vigorous wind does manage to disrupt some of the disk, dragging it out to form a cone within a much larger bubble. This provides a natural explanation for the difference in distribution between the outflow cone seen in Hα and the more extended X-ray emission. Without an early mild wind (models B1 and B2), the disk is disrupted before the wind has easy access to the halo, and so no obvious cone in the X-ray is visible. Even when present, the conical wind does not provide appreciable soft X-ray flux compared to the shocked halo (see Figs. 4, 10 and 14 in SBHL), so we would not expect to see such structures in the *ROSAT* data. The radial extent of the soft X-ray emitting material is much greater than that of the cones, the emission appearing more like a figure-of-eight (Fig. 4 in SBHL) or a cylinder (Fig. 10 in SBHL). None of the models SBHL present would be seen as more conical than cylindrical when projected along the line of sight and observed by a real X-ray instrument. As SBHL did not provide projected surface brightness plots, it is difficult to assess how limb-brightened the emission would be, but given the brightness of the shocked halo material it should be a detectable effect.

The luminosity varies greatly between the different models, and is not simply proportional to the mass and energy input in the starburst. Model A1 has a time averaged mass and energy input an order of magnitude less than model B1, but has a soft ($0.1 - 2.2$ keV) luminosity of $4 \times 10^{41}\,\mathrm{erg\,s^{-1}}$ at t = 16.6 Myr (when the starburst luminosity is $\sim 10^{44}\,\mathrm{erg\,s^{-1}}$, very close to M 82's bolometric luminosity), well above the $0.1 - 2.4$ keV wind luminosity of $\sim 2 \times 10^{40}\,\mathrm{erg\,s^{-1}}$ derived above for M 82. Model B1 has a corresponding X-ray luminosity of only $1.3 \times 10^{40}\,\mathrm{erg\,s^{-1}}$, despite having a similar initial gas distribution to model A1. Given the wide range of predicted wind luminosity it would require a deeper investigation of the available parameter space to use M 82's luminosity to constrain the allowable models.

SBHL provide "effective" temperatures for the gas in their "soft" band which corresponds well to the *ROSAT* band, by comparing fluxes in two energy bands of $0.1 - 0.7$ keV and $0.7 - 2.2$ keV, as well as the temperature range for the gas that provides the majority of the soft emission. In all cases the emission is very soft, typically $T \sim 0.2$ keV. The hottest model (B1) has a characteristic temperature of only 0.4 keV. This is still cooler than M 82's wind, where the temperature varies between $0.4 - 0.6$ keV. SBHL stress the lack of appreciable amounts of gas hotter than $\sim 6 \times 10^6$ K. The wind itself is much hotter, but provides very little emission, $L_X \sim 10^{38}\,\mathrm{erg\,s^{-1}}$. The lower temperatures predicted by SBHL do correspond with observations of some galaxies for which soft X-ray emission can be detected. NGC 891 has a halo with $T \sim 0.3$ keV (Bregman & Pildis, 1994), and Wang et al. (1995) detect soft ~ 0.25 keV X-ray emission out to more than 8 kpc from the plane of NGC 4631. A survey of *ROSAT* PSPC observation of nearby normal and starburst galaxies by Read et al. (1996) shows that many starbursts have diffuse gas with temperatures ~ 0.5 keV, more in line with our results.

The density of the gas responsible for the emission in SBHL's models is typically $n \sim 4 - 8 \times 10^{-2}\,\mathrm{cm^{-3}}$. This is not inconsistent with our results of $n_\mathrm{e} \sim 1 - 4 \times 10^{-2} \eta^{-1/2}\,\mathrm{cm^{-3}}$. The filling factor of the emitting gas in their models we can roughly estimate as ~ 0.1, which bring their densities close to ours. The gas mass providing the bulk of the soft emission depends strongly on the model used, but model B1 which has a soft X-ray luminosity similar to that observed for M 82's wind has a gas mass of $10^6\,M_\odot$, comparable with the total mass derived from the PSPC of $1.3 \times 10^7 \eta^{1/2}\,M_\odot$ for reasonable values of the filling factor.

6. Conclusions

We have provided a detailed spectral investigation of the extended soft X-ray emission associated with the starburst galaxy M 82. Point sources have been located and removed from the diffuse wind emission, and the effects of contamination by the nuclear source allowed for. The diffuse emission was divided into a set of distinct regions as a function of distance from the

galactic plane, allowing temperature, emission measure and absorbing column to be derived as a function of distance along the minor axis. The metallicity was found to be apparently low (0.00–0.07$Z_{\odot}$) throughout the wind, in agreement with results from ASCA. This work has shown the following:

- The observed soft X-ray morphology differs significantly between north and south, and is not well described as a conical outflow. The emission extends out to ~ 6 kpc from the plane of the galaxy. There is no evidence for any limb brightening, as would be expected if the soft emission came from the shock heated halo surrounding the hot wind.
- The emission from the wind is thermal. The temperature drops slowly along the wind, from ~ 0.6 keV near the nucleus, to ~ 0.4 keV in the outer wind. Numerical models of galactic winds predict the majority of the emission in the *ROSAT* band to be shocked halo, with effective temperatures in the range $0.2 - 0.4$ keV.
- Since the entropy of the gas is not constant, at least in the south, the observed emission cannot originate from a free wind itself. Our baseline analysis is based on an assumed cylindrical geometry, but a more divergent geometry only makes the southern wind less isentropic.
- The emission cannot come from a static halo of gas around M 82, given that the mass required to bind a hydrostatic halo is an order of magnitude higher than that inferred from the HI rotational velocity in the outer disk.
- For reasonable mass and energy input from the starburst, a simple model for emission from shock heated clouds using the observed density of the X-ray emitting gas to predict post-shock temperatures is consistent with the observed temperatures.

Acknowledgements. We thank the anonymous referee for valuable comments that have lead to the improvement of this paper. We acknowledge the use of the *Starlink* node at the University of Birmingham and thank the developers and maintainers of the X-ray analysis package ASTERIX. DKS and IRS gratefully acknowledge PPARC funding. This research has made use of data obtained from the UK ROSAT Data Archive Centre at the Department of Physics and Astronomy, Leicester University, UK, and the SIMBAD astronomical database at the CDS, Strasbourg.

References

Allan, D.J., 1995, ASTERIX User Note 004: Source Searching and Parameterisation. Univ. of Birmingham, Birmingham
Axon, D.J., Taylor, K. 1978, Nat, 274, 37
Bauer, F., Bregman, J.N. 1996, ApJ, 457, 382
Boggs, P.T., Byrd, R.H., Rogers, J.L., Schnabel, R.B. 1992, Applied and Computational Mathematics Division, U.S. Department of Commerce
Bregman, J.N., Pildis, R.A. 1994, ApJ, 420, 570
Bregman, J.N., Schulman, E., Tomisaka, K. 1995, ApJ, 439, 155
Cash,W. 1979, ApJ, 228, 939
Chevalier, R.A., Clegg, A.W. 1985, Nat, 317, 4
Collura, R., Reale, F., Schulman, E., Bregman, J.N. 1994, ApJ, 420, L63
Cottrell, G.A. 1977, MNRAS, 178, 577
Dekel, A., Silk, J. 1986, ApJ, 303, 39
Fabbiano, G. 1988, ApJ, 330, 672
Feigelson, E.D., Babu, G.J. 1992, ApJ, 397, 55
Freedman, W.L. et al. , 1994, ApJ, 427, 628
Götz, M., McKeith, C.D., Downes, D., Greve, A. 1990, A&A, 240, 52
Heckman, T.M., Lehnert, M.D., Armus, L. 1993 in The Environment and Evolution of Galaxies, J.M. Shull & H.A. Thronson, Jr (eds.), (Kluwer Academic Publishers, Netheralnds), 455
Heckman, T.M., Dahlem, M., Lehnert, M.D., Fabbiano, G., Gilmore, D., Waller, W., 1995, ApJ, 448, 98
Leitherer, C., Robert, C., Drissen, L. 1992, ApJ, 401, 596
McCarthy, P.J., Heckman, T.M., van Breugel, W. 1987, AJ, 92, 264
McKeith, C.D., Greve, A., Downes, D., Prada F. 1995, A&A, 293, 703
Muxlow, T.W.B., Pedlar, A., Wilkinson, P.N., Axon, D.J., Sanders, E.M., de Bruyn, A.G. 1994, MNRAS, 266, 455
Norman, C., Ikeuchi, S. 1989, ApJ,345, 372
O'Connell, R.W., Gallagher III, J.S., Hunter, D.A., Colley, W.N. 1995, ApJ, 446, L1
Ptak, A., Serlemitsos, P., Yaqoob, T. 1996, in "X-Ray Imaging and Spectroscopy of Cosmic Hot Plasmas", in press
Raymond, J.C., Smith, B.W. 1977, ApJS, 35, 419
Read, A.M., Ponman, T.J., Strickland, D.K. 1996, submitted to MNRAS
Rieke, G.H., Loken, K., Rieke, M.J., Tamblyn, P. 1993, ApJ, 412, 99
Schaaf, R., Pietsch, W., Biermann, P.L., Kronberg, P.P., Schmutzler, T. 1989, ApJ, 336, 722
Seaquist, E.R.,Odegard, N. 1991, ApJ, 369, 320
Snowden, S.L. et al., 1992, ApJ, 393, 819
Stark, A.A., Gammie, C.F., Wilson, R.W., Bally, J., Linke, R.A., Heiles, C., Hurwitz, M., 1992, ApJS, 79, 77
Suchkov, A.A., Balsara, D.S., Heckman, T.M., Leitherer, C. 1994, ApJ, 430, 511
Tomisaka, K., Bregman, J.N. 1993, PASJ, 45, 513
Tomisaka, K., Ikeuchi, S. 1988, ApJ, 330, 695
Trümper, J. 1984, Physica Scripta, 17, 209
Tsuru, T., Ohashi, T., Makishima, K., Mihara, T. 1990, PASJ, 42, L75
Tsuru, T. et al. 1996, in "X-Ray Imaging and Spectroscopy of Cosmic Hot Plasmas", in press
Wang, Q.D., Walterbros, R.A.M., Steakley, M.F., Braun, R. 1995, ApJ, 439, 176
Watson, M.G., Stanger, V., Griffiths, R.E. 1984, ApJ, 286, 144
Yun, M.S., Ho, P.T.P., Lo, K.Y. 1993, ApJ, 411, L17

This article was processed by the author using Springer-Verlag LaTeX A&A style file *L-AA* version 3.